Journal of Alloys and Compounds 968 (2023) 172030

Contents lists available at ScienceDirect

Journal of Alloys and Compounds

journal homepage: www.elsevier.com/locate/jalcom

Phase prediction, densification, and microstructure of $AlCrFeNi(TiO_2)_x$ high entropy alloy composite fabricated by spark plasma sintering

Samuel R. Oke [a,*], Oluwasegun E. Falodun [a], Abiodun Bayode [a], Ufoma S. Anamu [b], Peter A. Olubambi [b]

[a] Department of Mechanical Engineering, North-West University, Potchefstroom Campus, South Africa
[b] Centre for Nanoengineering and Advanced Materials, University of Johannesburg, Johannesburg, South Africa

ARTICLE INFO

Keywords:
Densification
Phase prediction
Microstructure
Spark plasma sintering
High entropy alloy

ABSTRACT

This study incorporates the knowledge of empirical calculation and computational concepts using Thermo-Calc as a design guide to develop AlCrFeNi high entropy alloy (HEA). Subsequently, a novel AlCrFeNi HEA composite consisting of varying weight percentages (wt%) of TiO_2 reinforcements is synthesized using mechanical alloying (MA) and spark plasma sintering (SPS) techniques. Our work investigated the role of TiO_2 reinforcement on the densification behavior, phase changes, microstructure, and properties of AlCrFeNi HEA. The phase diagram was constructed using Thermo-Calc software. Powder densification during SPS was analyzed using obtained sintering data. The samples were characterized using Xray Diffraction (XRD) and Scanning Electron Microscopy (SEM) techniques. The density and micro-hardness were evaluated. The result shows that the densification during SPS is dependent on kinetic mechanisms such as melt diffusion, surface diffusion, and plastic flow. Phases of the disordered BCC phase (rich in FeCr) and ordered B2 phase (rich in NiAl) were found in the AlCrFeNi HEA. The phases were consistent with the prediction using thermo-calc software. The BCC phases in the AlCrFeNi are retained regardless of the addition of TiO_2 particles but with the diffusion of Ti with O atoms fitting into the interstitial sites in the BCC and B2 lattice. The microstructure verified the homogeneous distribution of the TiO_2-rich phase within the BCC and B2 phases of the AlCrFeNi HEAs. The density decreases with the adding TiO_2. The hardness of reinforced AlCrFeNi is enhanced from 537.24 Hv to 752.74 Hv with an increment of TiO_2 reinforcement from 0 to 8 wt%. TiO_2 particles acted as impediments to the mobility of dislocation, thereby increasing the resistance to deformation of HEA composites during micro indentation.

1. Introduction

Metal matrixes reinforced with micro and nano-sized ceramic particles are promising materials with outstanding properties [1]. Composites of High entropy alloys are no exception; they have gained attention recently due to their exceptional structural stability and mechanical properties such as enhanced strength and hardness, outstanding fatigue resistance, excellent resistance to corrosion, and high thermal stability [2,3]. Though the primary core effects of sluggish diffusion, cocktail, high entropy, and lattice distortion have been reported to be the underlining mechanisms shaping the properties of HEAs [4–6], their practical strength and structure can be enhanced through dispersion and precipitation strengthening, solid-solution strengthening, pre-straining and grain refinement [7,8].

Past experimental evidence has revealed enhanced properties with dispersion strengthening and grain refinement [9]. So, exploring HEAs as a matrix for fabricating composite materials institutes a novel concept with possibly enhanced structure and engineering implications. Ceramic reinforcements, including TiB_2 [10], WC [11], Ti(C, N) [12], and Y_20_3 [13], have been extensively utilized as reinforcing phases to enhance the structure and properties of HEAs. Among these reinforcements, TiO_2 particles have emerged as promising reinforcement to enhance HEAs' structure compactness. In this context, TiO_2 is a filler within the HEA matrix, effectively improving its strength and hardness [14].

Furthermore, due to its favorable friction and wear resistance properties, TiO_2 finds widespread use as a surface coating material for metals [15]. The TiO_2 ceramic phase interacts with the HEA, forming a dense oxide layer that enhances the alloy's corrosion resistance [16]. Zhu et al. reported that adding TiO_2 ceramic phase to CoCrFeMnNi HEA improved wear, plastic deformation resistance, and reduced elastic

* Corresponding author.
E-mail address: sroke@futa.edu.ng (S.R. Oke).

https://doi.org/10.1016/j.jallcom.2023.172030
Received 31 May 2023; Received in revised form 4 August 2023; Accepted 3 September 2023
Available online 6 September 2023

Table 1
Thermophysical parameters of HEAs.

Parameter	Formula	Condition for solid-solution	References
Mixing Entropy (ΔS_{mix})	$-R\sum_{i=1}^{n}(c_i \ln c_i)$	$11 \le \Delta S_{mix} \le 19.5 J/k.mol$	[34]
Electronegativity difference ($\Delta\chi$)	$\sqrt{\sum_{i=1}^{n} c_i(x_i - \sum_{j=1}^{n} c_j x_j)^2}$	$\Delta\chi < 6\%$	[26]
Mixing enthalpy (ΔH_{mix})	$\sum_{i=1, i\neq j}^{n} \Omega_{ij} c_i c_j$	$-22 \le \Delta H_{mix} \le 7 kJ/mol$	[35]
Atomic size mismatch (δ)	$100\sqrt{\sum_{i=1}^{n} c_i(1-\frac{r_i}{r_a})^2}$	$\delta < 6.5\%$	[35]
Valence electronic configuration (VEC)	$\sum_{i=1}^{n} c_i (VEC)_i$	$VEC \ge 8.6$ for FCC $VEC < 6.87$ for BCC	[36]
Interacting parameter (Ω)	$\frac{T_m \Delta S_{mix}}{\lvert\Delta H_{mix}\rvert}$	$\Omega > 1$	[37]
Melting temperature (T_m)	$\sum_{i=1}^{n} c_i (T_m)_i$		[37]

The individual items involved are defined as. C_i (C_j) is the atomic percentage of the i-th $(j$-$th)$ component. r_i = atomic radius; $(VEC)_i$ = valence electron concentration; χ_i = Pauling electronegativity; T_m = calculated melting point through the atomic percentage; $\Delta G_{\max}$ = lowest (intermetallic) or highest (segregated) possible Gibbs free energy from the formation of binary systems.

recovery resistance [17]. In a related work by Qi et al., the strength of the $Al_{0.4}CoCrFe_2Ni_2$ HEA reaches the maximum of 489 MPa when reinforced with 2.5 vol% of TiO_2 ceramic phase, which is 11.1 % higher than the matrix HEA [14]. Chang et al. added varying amounts of TiO_2 particle addition, and their findings demonstrated that adding TiO_2 particles resulted in the prevalence of grain refinement and improved strength without significant loss in elasticity [18]. These studies position TiO_2 as an attractive candidate for fabricating HEA composites. Despite the potential benefits, there are still limited reports on HEA/TiO_2 composites, making further investigation necessary.

Amongst HEAs, Al-Co-Cr-Cu-Fe-Ni systems are among the most studied due to their enhanced performance [19]. The deterioration in mechanical properties due to Cu segregation shifted the research focus towards synthesizing Al-Co-Cr-Fe-Ni systems. The removal of Cu element advanced the strength of the HEA [20]. Many investigations have also targeted substituting Co with other metals because of its magnetic nature and toxicity [21]. Further elimination of Co from the Al-Co-Cr-Fe-Ni system created the Al-Cr-Fe-Ni HEAs. The removal of elements from HEAs has been reported to influence the microstructure and properties of HEAs significantly. For example, Munitz et al. [22] investigated the influence of the removal of Co from the microstructure of as-cast AlCoCrFeNi alloys. They reported that the as-cast AlCrFeNi system had a eutectic-like microstructure that yielded outstanding strength and elasticity. Works of literature exist on AlCrFeNi HEAs [23–25], but there are few reports on its composites. Thus, this study endeavors to disperse TiO_2 ceramic particles within the AlCrFeNi alloy, aligning with the HEA design concept, and subsequently explores the resulting variations in composite microstructure and properties.

Among various fabrication techniques for Al-Cr-Fe-Ni HEAs, arc melting is the conventional method of synthesizing this class of HEAs. But this technique is unsuitable for fabricating HEAs reinforced with ceramics particles due to substantial elemental segregation that occurs due to differences in melting points of metallic elements and ceramics [26]. Pores and shrinkage defects in HEAs are also characteristic of arc melting. The powder metallurgy (PM) route has been reported to be a more efficient method for the fabrication of HEAs composites due to its advantages of even compositions, uniform microstructures, and small grain sizes [27,28]. For this study, SPS was utilized to fabricate the HEA reinforced with different percentages of TiO_2. The choice of SPS over other PM routes is due to the advantages of low temperature and shorter sintering time, grain growth annihilation due to the fast-cooling rate of SPS, and the production of fully dense materials [29,30]. Until now, many investigations have been tailored toward the properties and microstructures of various PM HEAs. Still, few studies have been reported on the densification mechanism during SPS.

Advancements in HEA production and processing have introduced computational tools like CALPHAD-based techniques to aid in designing, modeling, and simulating HEAs' thermodynamic properties [31]. This paradigm shift in alloy development has formed an integral part of materials research, driven by the fourth industrial revolution (4IR). The vast compositional space of HEAs necessitates integrating computation-aided materials design, specifically Thermo-Calc software (a CALPHAD-based tool), in the materials design and optimization process [32]. As opposed to the conventional approach for HEA development, empirical calculations are complimented by the computational design process; the core features of the non-conventional process will not only eliminate the trial-by-error menace associated with the traditional experimental approach but will create a framework that will minimize materials waste and consequently enhance production time and high yield [33].

This study, therefore, incorporates the knowledge of empirical calculation and computational concepts using Thermo-Calc as a design guide to develop solid-solution AlCrFeNi HEA before the synthesis of a novel AlCrFeNi HEA-based composite consisting of TiO_2 reinforcements using mechanical alloying and spark plasma sintering techniques. It provides an effective way of uniformly dispersing oxide particles into AlCrFeNi HEA. The role of TiO_2 addition on the microstructure, phase changes, and densification behavior of the HEA throughout the sintering process is emphasized.

2. Experimental procedure

2.1. Theoretical design of HEA

Empirical calculations brewed from thermo-physical parameters (as captured in Table 1), and Thermo-Calc software version 2021b with the Thermo-Calc High Entropy Alloy version 4 (TCHEA4) encrypted thermodynamic database was used in the phase diagram modeling and phase prediction of the quaternary equiatomic (Al-Cr-Fe-Ni) HEA. For the seamless design of alloys, especially HEAs, scores of researchers have adopted the non-conventional approach involving empirical calculations and computational modeling in computing and predicting the thermodynamic properties and structural behavior of material systems. Some of the thermophysical design parameters applied in literature in the design of solid-solution HEAs are summarized in Table 1.

2.2. Mechanical alloying and Spark plasma sintering of the AlCrFeNi HEA and its composites

The starting metallic powders utilized are HEA in this study are high

Table 2
Thermophysical properties of designed AlCrFeNi HEAs.

HEA	Nominal ρ (gcm^{-3})	Structure	*VEC*	ΔH_{mix} ($kJmol^{-1}$)	ΔS_{mix} ($kJmol^{-1}$)	T_m (oC)	δ (%)	Ω	Δx
Al-Cr-Fe-Ni	6.271	BCC	6.75	-21.0173	11.52566	1595	2.84	0.87	0.12

purity Al (99.95 %; Sigma-Aldrich), Cr (≥99 %, Sigma-Aldrich), Fe (99.5 %, Merck), and Ni (99.7 %, Merck) in equal atomic proportions (25 at %). Titanium IV oxide (TiO_2) ceramic powder of 99.9 % purity, supplied by Merck Co., is introduced in varied proportions as reinforcements (2–8 wt%). The Metallic powders were measured according to calculated amounts and introduced into a milling pot for mechanical alloying. The process employed a QM-3SP4 Planetary Ball Mill, utilizing balls with a ball-to-powder weight ratio of 10:1. Equiatomic HEA powders were achieved after 24 h of vacuum milling at 150 rpm. The TiO_2 powders were later introduced into the mixed HEA powders and successively subjected to another 8 h of dry milling to obtain a homogenous blend of AlCrFeNi$(TiO2)_x$ powders. To avert cold welding arising from powder overheating, a relaxation time of 10 mins was incorporated after every 20 mins of milling. This strategy mitigates interfacial reactions among the AlCrFeNi(TiO2)x powders during milling.

The admixed AlCrFeNi$(TiO2)_x$ powders are loaded in a 20 mm diameter graphite punch and die assembly and cold compacted at 10 MPa using the hydraulic press. The AlCrFeNi$(TiO2)_x$ compact was then consolidated using spark plasma sintering (HHPD– 25 FCT model, Germany). The compact was sintered in a vacuum at 1100 °C, pressure, 10 mins holding time, and 100 °C/min heating rate. The applied pressure of 50 MPa was kept constant throughout the sintering cycle. A graphite sheet was used to shield the powders from direct contact with the die and punches to ensure enhanced electrical conductivity and easy removal of the sinter after sintering. After sintering, AlCrFeNi(TiO2)x composite with 20 mm diameter and 10 mm height was attained. The sinter was sand blasted to remove dirt and sticky graphite sheets from the HEA. The sintering data obtained after SPS was used in the study to analyze the densification mechanism throughout the sintering process.

2.3. Characterization of the sintered AlCrFeNi HEA and its composites

The sizes and shapes of individual starting powders, the degree of dispersion among admixed powders, and the microstructure of the fabricated AlCrFeNi$(TiO2)_x$ composites were examined using a scanning electron microscope (SEM). For the microstructural evaluation, the AlCrFeNi$(TiO2)_x$ sintered samples were cold mounted to allow easy grinding and polishing. Metallographic preparation of the sample's surface was done to achieve a mirror-like consistency. The AlCrFeNi (TiO2)x composites' chemical constituents were analyzed using energy-dispersive X-ray spectroscopy (EDS). The SEM utilized in this study was equipped with an energy-dispersive detector. The crystal structure and analysis of phases of the AlCrFeNi$(TiO2)_x$ powder mixture after MA and the sintered samples were evaluated using an X-Ray diffractometry (XRD, PANalytical EMPYREAN) using Cu Kα radiation. The X-ray diffractions were recorded in the range of 5 – 100° at 2 θ angles with a scan rate of 1.0 deg/min.

2.4. Density and hardness measurements of the sintered AlCrFeNi HEA and its composites

The sintered HEA composites' resistance to micro indentation was assessed using a Vickers hardness tester (FALCON 500 series). Samples underwent surface polishing, and indents were created across various

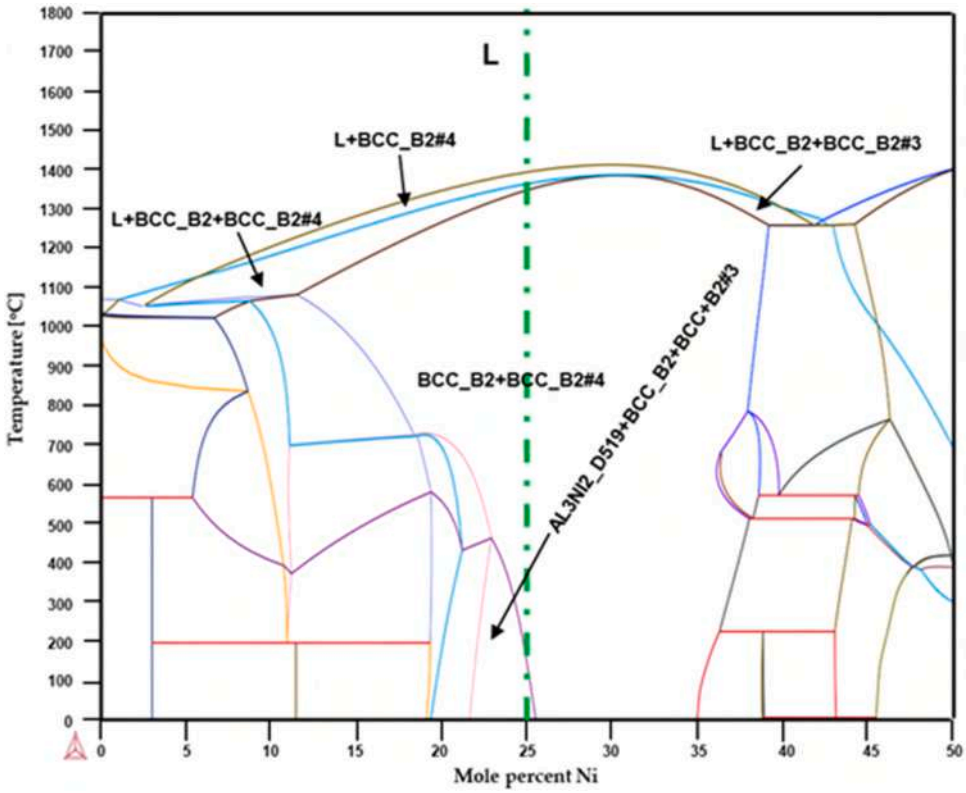

Fig. 1. T-C phase diagram of quaternary equiatomic (Al-Cr-Fe-Ni) HEA.

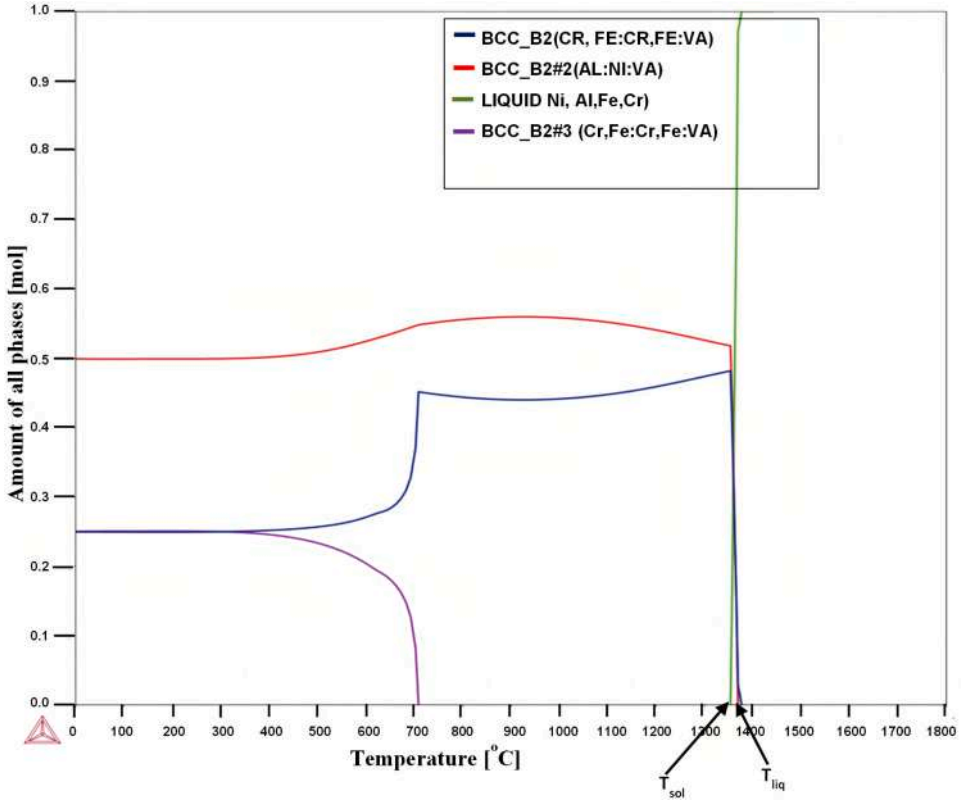

Fig. 2. The phase composition of equiatomic Al-Cr-Fe-Ni HEA across the temperature range.

regions with a 100 gf load for 10 s. The results were obtained by recording the indenter tip's penetration into the sample surface. Data reliability was ensured through 10 repeat tests.

The relative density of the AlCrFeNi(TiO2)$_x$ composites was calculated using the theoretical and experimental densities of the sample. The AlCrFeNi(TiO2)x samples' theoretical density was calculated using Eq. (1).

$$\frac{1}{D_c} = \frac{Vf_{HEA}}{D_{HEA}} + \frac{Vf_{TiO2}}{D_{TiO2}} \quad (1)$$

where D_c is the theoretical density of AlCrFeNi(TiO2)$_x$, D_{HEA} and D_{TiO2} denote the theoretical densities of the AlCrFeNi, and the TiO_2 reinforcement, $Vf_{HEA,}$ and Vf_{TiO2} are the volume fractions of the AlCrFeNi and the TiO_2 reinforcement respectively. Archimedes' principle was used to estimate the experimental densities of the sintered samples in compliance with ASTM B962. The relative density of the AlCrFeNi (TiO2)$_x$ composites was finally calculated using Eq. (2).

$$Relative \quad density \quad (\%) = \frac{Experimental \quad density}{Theoretical \quad density} X100 \quad (2)$$

3. Results and discussion

3.1. Construction of phase diagram and phase prediction for the AlCrFeNi HEA

Adopting the designated formulas highlighted in Table 1 for the alloy design, the quaternary equiatomic AlCrFeNi's thermophysical properties were computed and reported in Table 2.

Notably, the values obtained for all the computed parameters lie within the phenomenological range, as expected in developing a solid-solution high entropy alloy. Empirical calculation from the thermophysical parameters may not be overly depended upon because it strongly relies on the availability of experimental data from the literature for alloy design. Also, most benchmarked threshold values for the various parameters computed empirically are only based on statistics and lack scientific backing. Since empirical rules are not conclusive in predicting solid solution phases in HEAs, CALPHAD-based tools have attracted strong recommendations by alloy developers for their self-consistent, reliable, accurate, and easy-to-use capabilities. Thermo-Calc, among other CALPHAD-based tools, stands out as software that can appropriately be used to model phase diagrams and predict the thermodynamic properties of alloys. Fig. 1 depicts the temperature-composition (T-C) phase diagram of the quaternary equiatomic (Al-Cr-Fe-Ni) HEA calculated using Thermo-Calc software version 2021b.

Being an equiatomic HEA, each principal element has 25-mole percent as the composition, with the isopleth line representing the specific composition site indicated with a green dash-dotted line across the alloy composition to varied temperatures. Using the software's graphical user interface (GUI) mode, the system condition was set at room temperature (T_{room}) to 1800 °C and at a pressure of 1 bar. Across the isopleth line, a series of possible reactions to changes in temperature upon cooling was identified as summarized below:

$$(L) \rightarrow (L + BCC\_B2\#4)$$

$$(L + BCC\_B2\#4) \rightarrow (L + BCC\_B2) + (BCC\_B2\#4)$$

$$(L + BCC\_B2) + (BCC\_B2\#4) \rightarrow (BCC\_B2) + (BCC\_B2\#4)$$

$$(BCC\_B2) + (BCC\_B2\#4) \rightarrow (Al3Ni2\_519) + (BCC\_B2) + (BCC\_B2\#3)$$

Fig. 2 was computed using the One-axis plot to obtain information on the phases present and their respective number of phases in the equiatomic Al-Cr-Fe-Ni HEA across various temperatures. It also provides information concerning the liquidus temperature (T_{liq}) and solidus temperature (T_{sol}).

The predicted stable phases obtainable in the cooling curve diagram for the quaternary equiatomic (Al-Cr-Fe-Ni) HEA are BCC_B2 (blue

Table 3
Thermo-Calc predicted calculations for equiatomic Al-Cr-Fe-Ni HEAs upon cooling.

Stable phases	Constituent elements	Amount in mole%	Temperature range (°C)
BCC_B2	Cr,Fe:VA	45	≃ 1375 - T_{room}
BCC_B2#2	Ni,Al:VA	55	≃ 1370 - T_{room}

colored line) and BCC_B2#2 (red colored line) phases, whereas BCC_B2#3 (lilac colored line) phase which precipitated at about 710 °C was identified in the reaction but later dissolves into the BCC_B2#2 stable phase. Further deduction from the cooling curve diagram shows that the solidification temperature (T_{sol}) begins at about 1355 °C, where BCC_B2 and BCC_B2#2 phases co-exist. Table 3 presents a concise summary of the predicted stable phases. BCC_B2 phase is rich in both Cr and Fe and takes approximately 45 % of the system. This phase is formed at around 1375 °C and sustains stability below the room temperature mark. The BCC_B2#2 phases, on the other hand, precipitated at about 1370 °C, and were maintained below room temperature. It occupies 55 mol percent of the entire phase of the HEA system, with the primary constituent elements being Ni and Al and a moderate inclusion of Fe. Thermo-Calc software's thermophysical parameter calculations and prediction suggest that the AlCrFeNi HEA is a BCC solid-solution system.

3.2. Characterization of the starting and mixed powders

The morphology of the Al, Cr, Fe, Ni, and TiO_2 as-received powders is depicted in Fig. 3(a-e), respectively. The SEM analysis of the powders revealed different particle sizes and shapes of the powders. The Al powders with particles size of < 75 μm μm have non-porous, spherical shapes. The Cr and Fe powders have average particle sizes of 45 μm and 325 mesh, respectively, characterized by irregular and flake-shaped particles. The Ni particles exhibit flake-like morphology, with average particle sizes mostly around 2.7 μm. The reinforcing TiO_2 particles are round with a hollow doughnut-like morphology with an average particle size of 35 μm. Mixing spherical and flake-shaped powders can enhance composite properties. Spherical powders boost packing density, while flakes offer anisotropic reinforcement and controlled fracture [38]. Particle size is crucial for improved microstructure and properties. The choice of micron-sized powders for the HEA composites allows for efficient milling and good densification during sintering, resulting in desirable properties in the final material. Micron-sized powders are more cost-effective than submicron-sized powders and are easily handled during processing. Macía et al. investigated micron-sized particles' influence on ferritic ODS steel milling and consolidation with (Y–Ti–Al–Zr). They reported even temperature distribution, advancing recrystallization, and promoting efficient consolidation [39]. Fig. 1f depicts XRD analysis of TiO_2, confirming rutile crystal phase presence with a tetragonal structure.

The challenge of fabricating HEA composites with improved properties is to create a uniform dispersion of the metallic and reinforcement powders. The degree of dispersion of the powders is assessed, and the morphology and elemental compositions (EDX) of the admixed AlCrFeNi$(TiO2)_x$ powders after mixing are presented in Fig. 4. As observed in the micrographs, the mechanical alloying parameters employed resulted in homogenous dispersion of the Al, Cr, Fe, and Ni metallic powders (Fig. 4a) and with TiO_2 reinforcements (Fig. 4b). There is no observed fragmentation or agglomeration of powders. The effective distribution of powders with no deformation could be attributed to the absence of milling balls during powder blending. The EDS for Fig. 4a of the unreinforced AlCrFeNi revealed only peaks corresponding to Al, Cr, Fe, and Ni, with no additional element observed. This ascertains no substantial contamination of the HEA powders during mixing. The presence of a Ti peak was observed for the reinforced AlCrFeNi(TiO2)x (EDS for Fig. 4b).

The XRD diffraction peaks of the AlCrFeNi HEA powder with varied addition of TiO_2 after 30 h of milling are presented in Fig. 5. The distinctive Bragg's peaks of single BCC crystal structure were identified with Al and Ni pure elements, and this validates the predicted results from both the empirical calculation with a VEC value of 6.75, indicating a BCC phase structure, and the Thermo-Calc design that also specified a BCC material along the isopleth line. Though Shang et al. reported the complete dissolution of Al and Ni elemental powders resulting in an absolute BCC structure of AlCrFeNi HEA after 30 h of milling, the emergence of Al and Ni elements could be linked to the difficulty associated with fracturing spherical powders during MA. Diffraction peaks corresponding to TiO_2 with different 2θ values are also identified in AlCrFeNi$(TiO2)_x$ composite grades. The disappearance of elemental

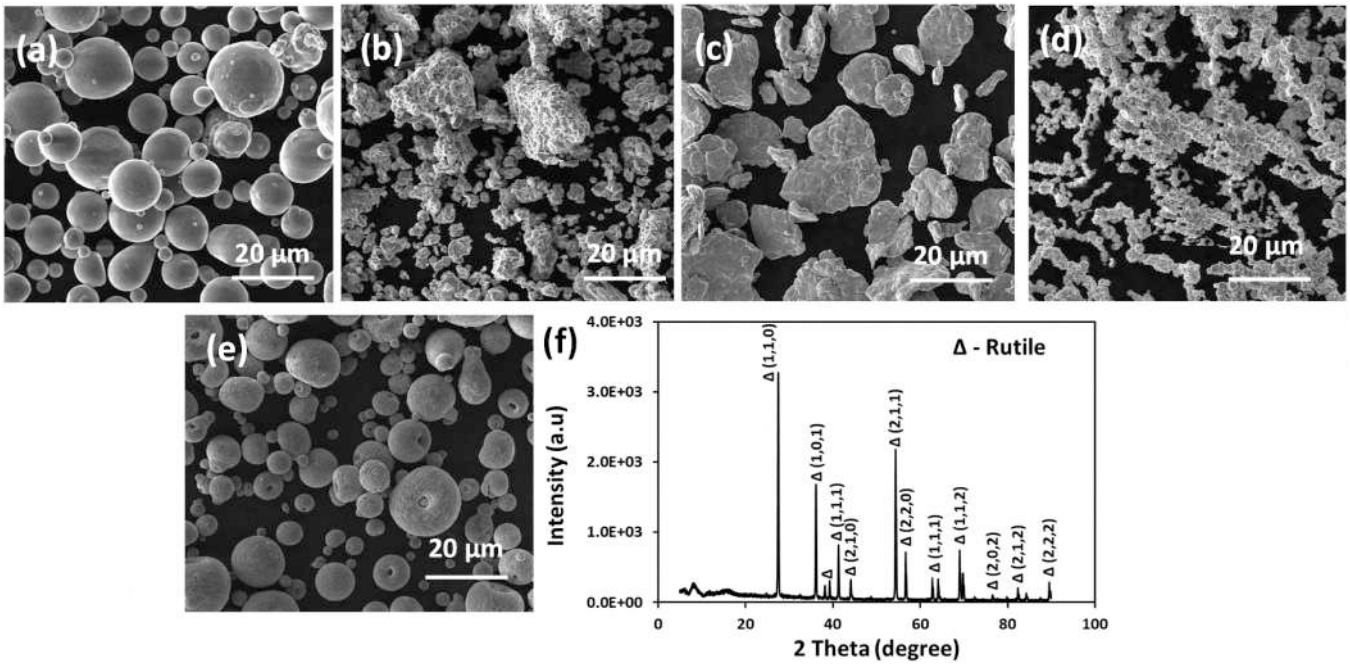

Fig. 3. SEM micrographs of the elemental powders morphology (a) Al, (b) Cr, (c) Fe, (d) Ni, (e) TiO_2, and (f) XRD of TiO_2.

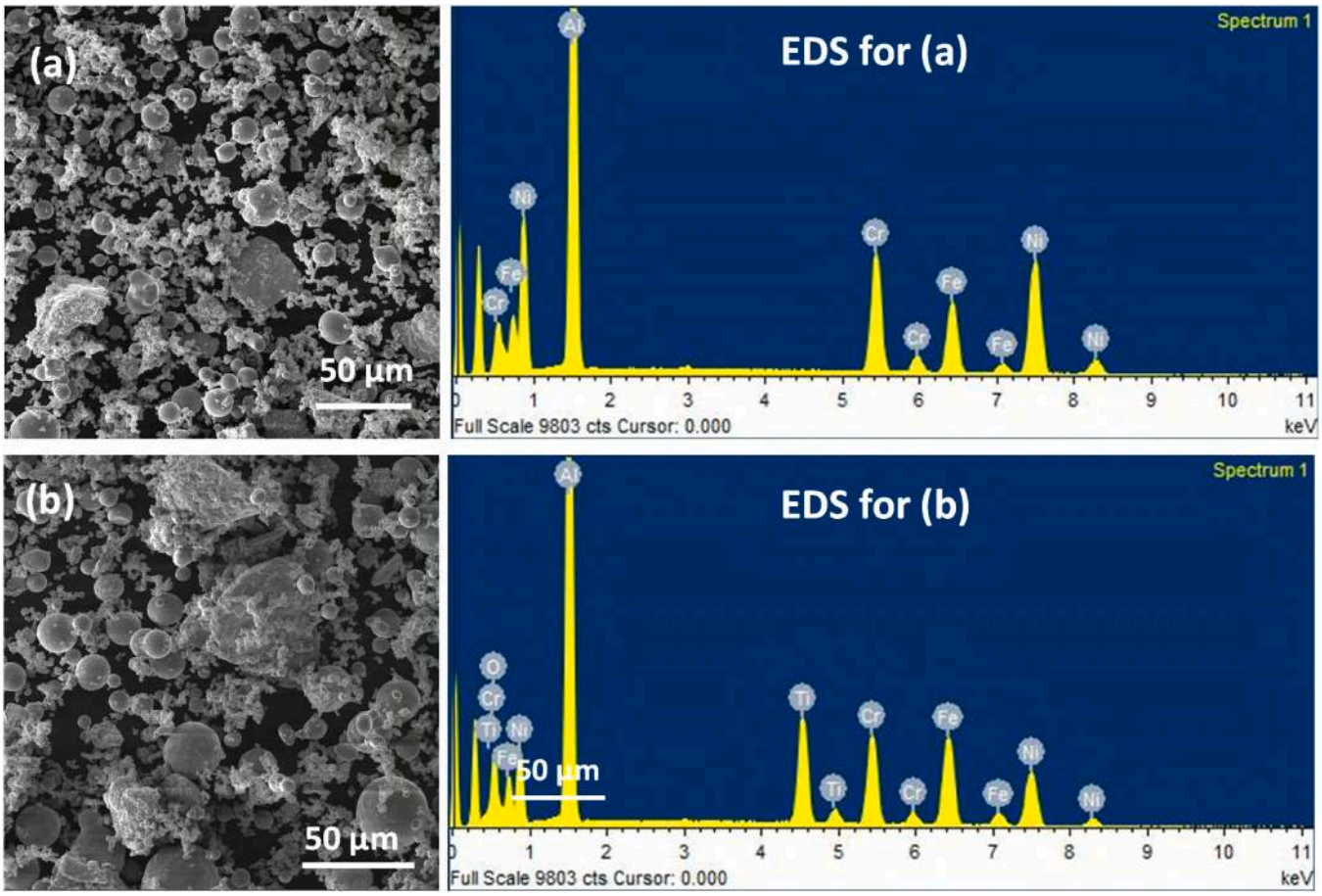

Fig. 4. SEM and EDS results for mixed AlCrFeNi powders (a) 0 wt% TiO_2 and (c) 4 wt% TiO_2.

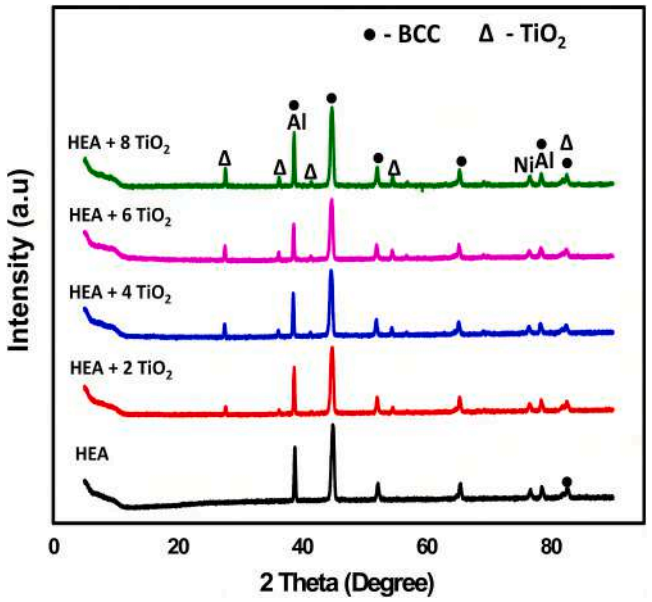

Fig. 5. XRD results of mixed AlCrFeNi with various TiO_2 powders.

peaks in the formation of BCC crystal structure in HEAs has been reported to be due to crystal size refinement, decreased crystallinity, and lattice distortion [40].

3.3. Sintering behavior of the sintered AlCrFeNi HEA and its composites

Fig. 6a depicts the variation in temperature with time, and Fig. 6b presents the variation in the relative displacement rate of the punch during the deformation of the powders in the SPS machine. The sintering profiles for the AlCrFeNi and its composites displayed a similar trend. The sintering temperature (Fig. 6a) remained constant at 250 °C (due to sintering chamber preheating) for approximately 6–8 min and then gradually increased to a maximum of 1100 °C and held for 7 min. This duration represents the adopted holding time for the sintering process of the composites. The profile also shows that the sintering process was completed in 30 min with the attainment of near-total densification. The short time of sintering demonstrates the efficiency of SPS compared to conventional sintering techniques [41]. Fig. 6b indicates the regime of compression exerted by the upper and lower punch to reduce the powder from its initial height (h_0) to the final sinter height (h_i) during SPS. The first 10 mins of sintering recorded a low punch displacement; this could result from the resistance to deformation posed by the powders due to low temperature (Fig. 6a). From 10–25 mins of sintering, displacement gradually increased from 1 to about 3 mm. This indicates that the deformation of the AlCrFeNI remarkably occurs between 10 and 25 mins. No significant increase in displacement was recorded in the last 5 mins. The displacement is significantly higher in of AlCrFeNi compared to the composite powders. This high displacement can be attributed to more interconnected pores in the AlCrFeNI samples.

The variation of the shrinkage rate with time was examined during the SPS process, as depicted in Fig. 7. The maximum shrinkage rates for all the HEA composite grades were achieved in 10 mins of sintering. It is important to note that the maximum sintering temperature (1100 °C) was not attained in 10 mins of sintering. So, the dominant process

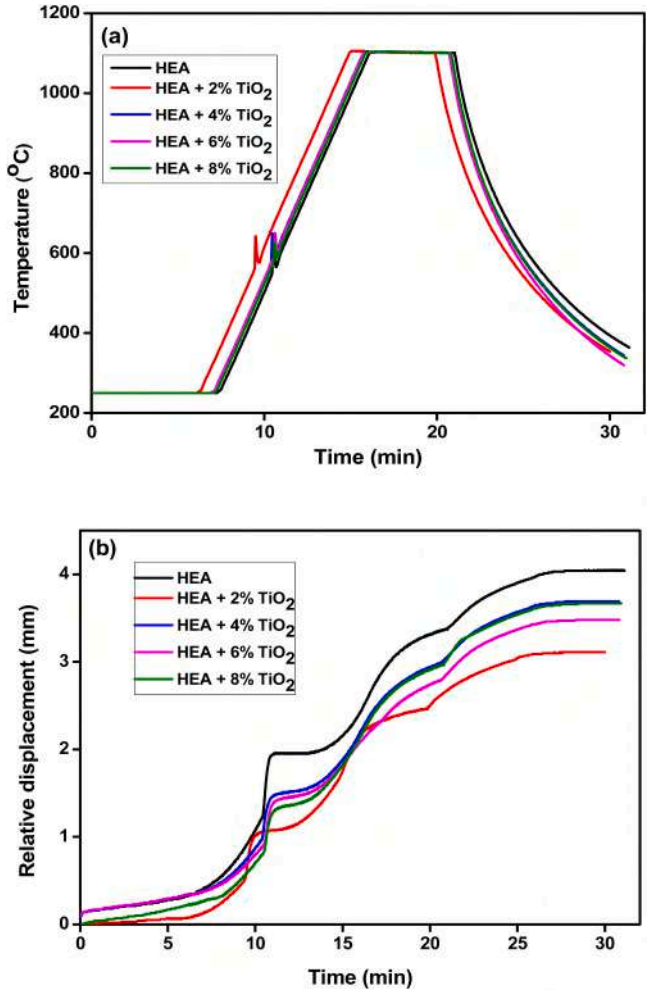

Fig. 6. Variation of (a) sintering temperature and (b) punch relative displacement as a function of time during deformation of HEA powders during sintering.

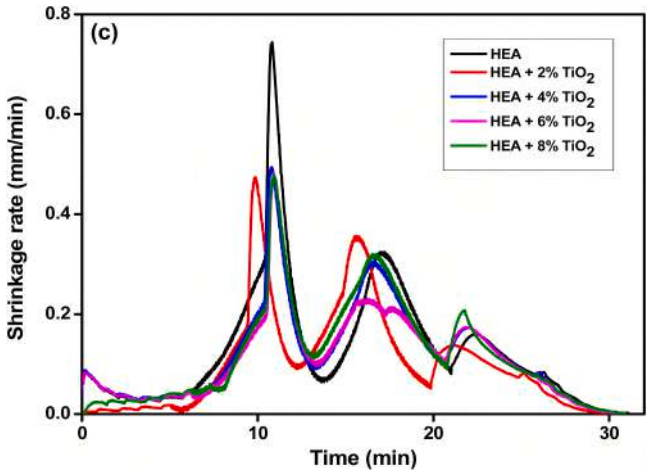

Fig. 7. Shrinkage/deformation of the mixed AlCrFeNi HEA and TiO_2 powers with time during SPS.

parameter that influenced the high shrinkage rates of the HEAs is the sintering pressure maintained at 50 MPa. This stage is characterized by a severe decrease in powder bed height, removal of gas, and spark creation between HEA and TiO_2 particles. The shrinkage rate of the HEA

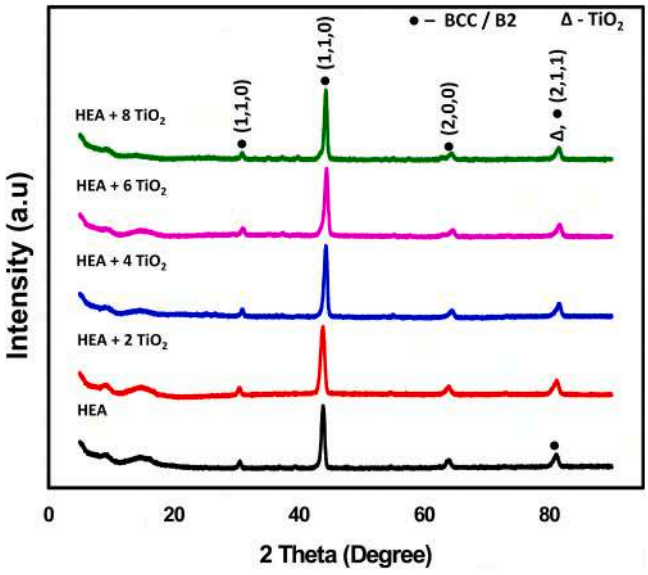

Fig. 8. XRD results of sintered AlCrFeNi and its composites reinforced with various amounts of TiO_2.

without TiO_2 reinforcement appeared to be higher (0.74) compared to other reinforced grades. A drastic reduction in shrinkage rate from 0.74 to 0.42 was observed by adding 2 wt% TiO_2 particles. Further addition of TiO_2 particles did not significantly affect the shrinkage rate. The high shrinkage rate in the HEA without TiO_2 suggests a high sinter density with low porosity. The remarkable difference in shrinkage rate could be linked to the nature of the SPS mode of heating which favors self-heating by microscopic discharge between HEA particles. This results in a significant amount of rapid transfer of heat. The reduced shrinkage rate with the addition of TiO_2 could be attributed to the difference in thermal conductivities of the HEA and the TiO_2 particles. The TiO_2 tends to slow the rate of electron discharge that is liable to initiate local heating of particles, so the rate of melting of particle surface is lowered. Densification during SPS has been reported to depend on kinetic mechanisms such as melt diffusion, surface diffusion, and plastic flow [42].

3.4. Phase evolution of the sintered AlCrFeNi HEA and its composites

The peaks corresponding to diffraction patterns of the sintered HEA and HEA-TiO_2 (2 – 8 wt%) in the 2 θ range of 0 – 100° are depicted in Fig. 8. The HEA and composites observed diffraction patterns corresponding to the disordered BCC phase (rich in Fe, Cr; JCPDS 34-0396) and ordered B2 phase (rich in Ni, Al; JCPDS 44-1188). This implies that the BCC phase in the AlCrFeNi is retained regardless of the addition of TiO_2 particles. The occurrence of the BCC and B2 phases is supported by the predicted HEA phase diagram reported in Fig. 1. Peng et al. [43] used MA and SPS to fabricate AlCrFeNi reinforced Y_2O_3/Ti; similar Ni-Al enriched ordered B2 phase, and Fe-Cr enriched disordered BCC phase results were reported. The resulting phases were attributed to spinodal decomposition in the matrix during sintering. Fig. 8 clearly shows that the lattice parameters, orientation, and crystal structures of BCC disordered and B2 ordered phases are alike, resulting in overlapping their diffraction peaks. Diffraction peaks relating to the TiO_2 phase (JCPDS No. 21-1276) are not evident in the HEA reinforced with 2 wt% TiO_2. The complex phenomena of densification, creep, deformation, and mass diffusion associated with SPS could result in the diffusion of Ti with O atoms fitting into the interstitial sites in the BCC and B2 lattice [44]. With the addition of TiO_2 beyond 2 wt%, diffraction peaks corresponding to TiO_2 were recorded with more Ti and O atoms available for incorporation into the BCC and B2 lattice of AlCrFeNi. This suggests that the AlCrFeNi matrix becomes supersaturated, reaching a point where it

Table 4
Chemical composition (in weight percent, wt%) of sintered AlCrFeNi and its composites reinforced with various amounts of TiO_2.

Elements	HEA	HEA-2TiO_2	HEA-4TiO_2	HEA-6TiO_2	HEA-8TiO_2
Al	17.35	20.52	18.54	15.37	17.29
Cr	41.14	31.43	24.77	28.67	25.95
Fe	20.03	18.70	20.44	19.08	18.34
Ni	15.48	17.31	15.01	16.90	13.62
Ti	-	5.22	7.56	10.13	11.74

cannot accommodate any more Ti and O atoms within the BCC and B2 lattice during the SPS process. As a result, the excess Ti and O elements form precipitates in the form of additional TiO_2. Table 4 presents the results of the EDS analysis, which aimed to determine the elemental composition of the pure AlCrFeNi and its composites reinforced with varying amounts of TiO_2. The analysis revealed that the diffusion of Ti atoms into the HEA matrix was more noticeable when higher concentrations of TiO_2 were employed.

Fig. (9a) presents the diffraction patterns of the sintered AlCrFeNi compared with as-milled AlCrFeNi powder. In contrast, Fig. (9b) shows diffraction patterns of the sintered AlCrFeNi reinforced with TiO_2 compared with as-milled powder of the same TiO_2 volume fraction. The Al and Ni in the milled AlCrFeNi dissolved utterly into the BCC/B2 phase (Fig. 9a). The dissolution of Al and Ni in the BCC phase during SPS at high temperatures occurs due to the compatibility of the BCC lattice structure with Al and Ni atoms and increased thermal energy facilitating

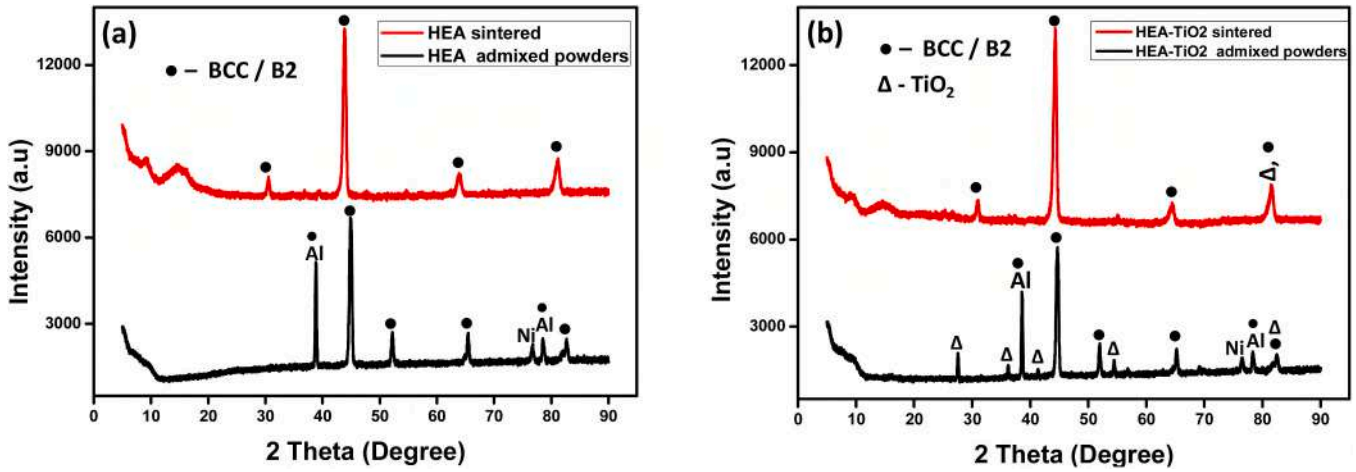

Fig. 9. Comparison of (a) XRD of HEA admixed powder and Sintered HEA without TiO_2 (b) XRD of HEA admixed powder and Sintered HEA with TiO_2 addition.

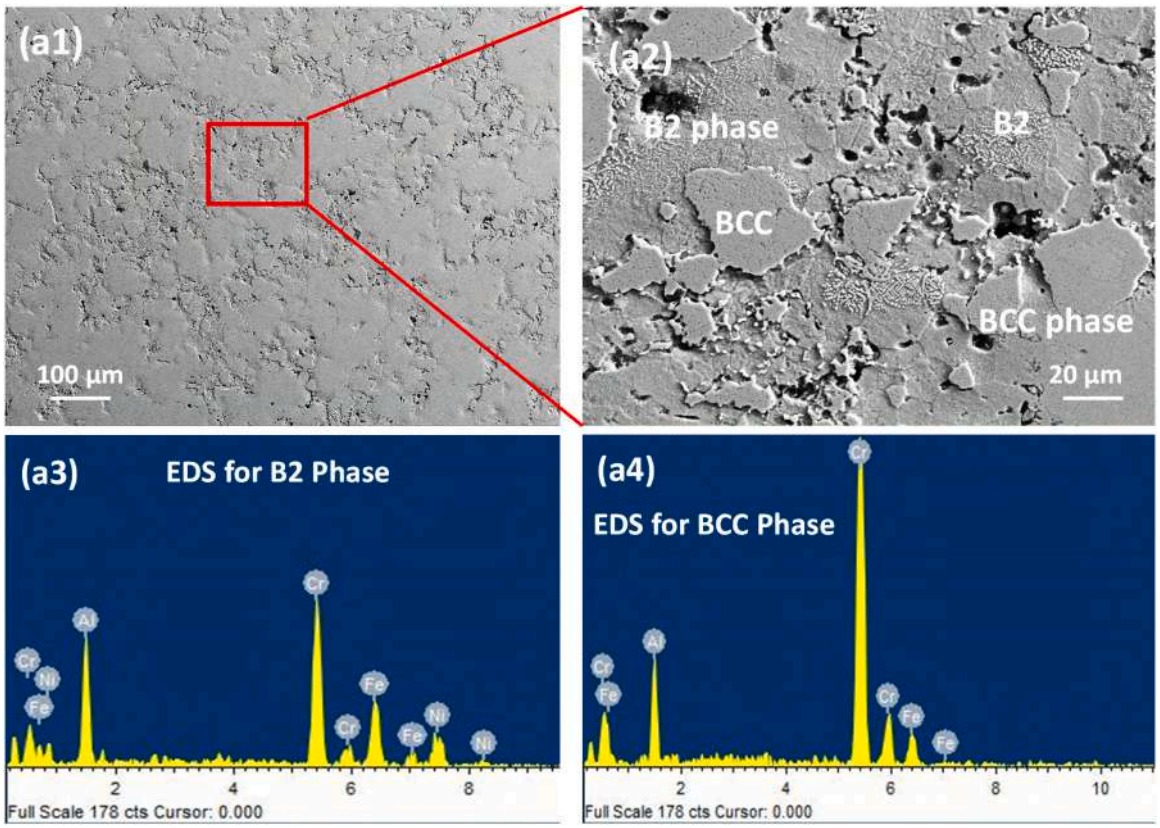

Fig. 10. Microstructure and elemental distribution of the sintered AlCrFeNi HEA without TiO_2.

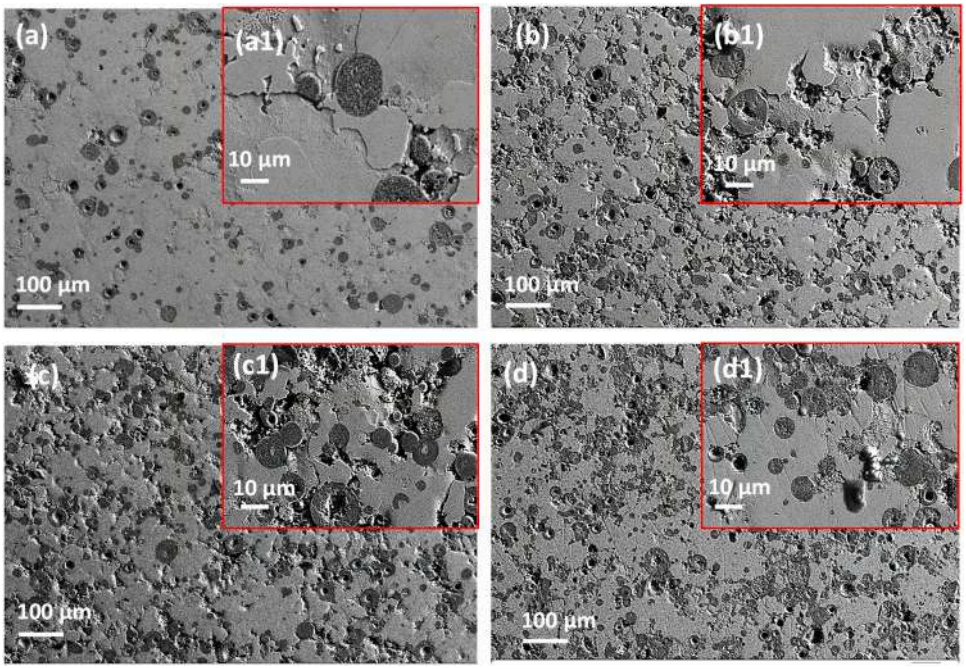

Fig. 11. Microstructure of the sintered AlCrFeNi HEA reinforced with 2, 4, 6, and 8 wt% TiO_2 represented as (a) – (d) respectively.

atomic movement and diffusion. This phenomenon leads to solid solubility, where Al and Ni atoms become uniformly distributed within the BCC lattice. In Fig. (9b), the peaks corresponding to TiO_2 (28°, 37°, 42°, 55°) in the milled powder were observed to disappear after sintering. The TiO_2 peak is only evident at 82°. The non-appearance of the TiO_2 peaks could be linked to two factors. Firstly, it is imperative to state that the TiO_2 particles will not melt during sintering due to its high melting temperature of 2116 K, but the Ti atoms can diffuse into the BCC lattice of the AlCrFeNi as substitutional atoms to form AlCrFeNiTi HEA. Secondly, it could be due to the low volume of TiO_2, which is below the resolution limit of the XRD device.

3.5. Microstructures of the sintered AlCrFeNi HEA and its composites

Fig. 10 (a1 and a2) shows the SEM images at low and high magnifications of sintered AlCrFeNi without reinforcement. The alloy comprises two regions corresponding to the BCC and B2 phases, as labeled in the micrograph. The resulting EDS, which shows the elemental composition of the two regions (B2 and BCC), is presented in Fig. 10 (a3) and (a4), respectively. The BCC of the AlCrFeNi high-entropy alloy (HEA) exhibits a significant abundance of Fe and Cr elements, aligning with the composition of the [Fe, Cr] solid solution identified through X-ray diffraction (XRD) analysis. Likewise, the B2 phase within the alloy

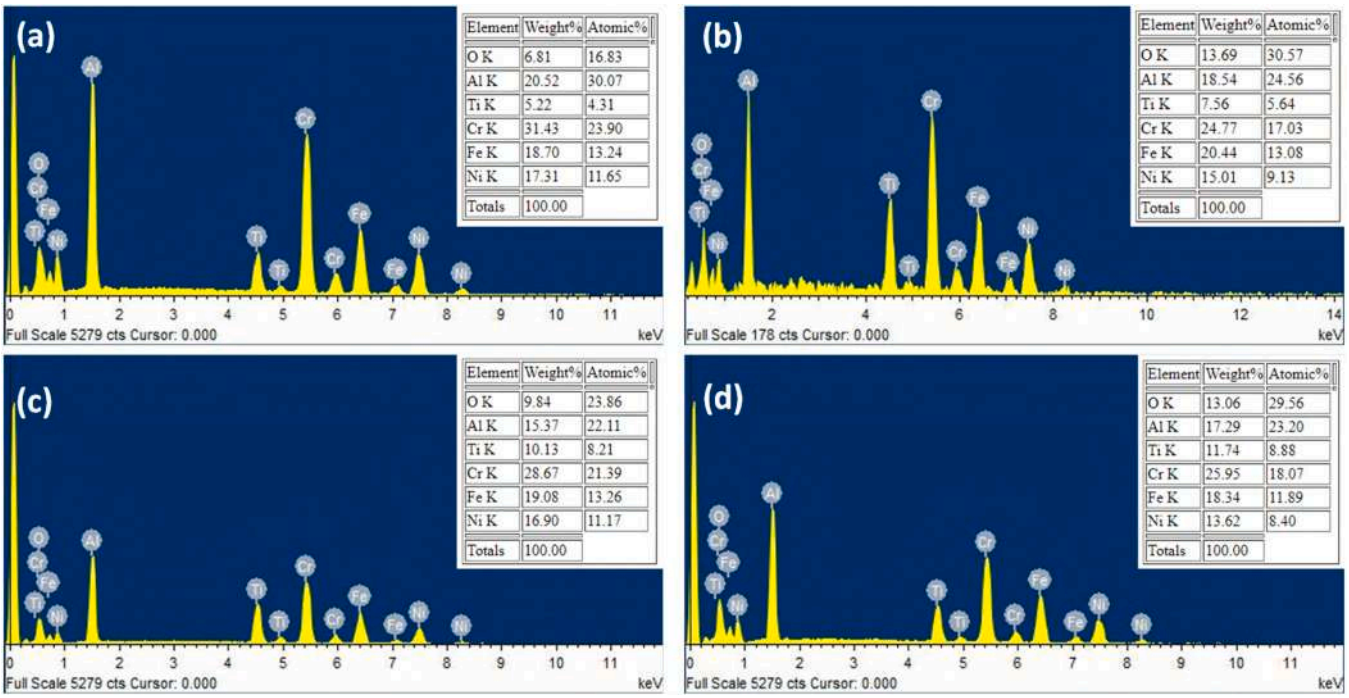

Fig. 12. EDS showing the elemental composition of the sintered AlCrFeNi HEA reinforced with 2, 4, 6, and 8 wt% TiO_2 represented as (a) – (d), respectively.

Table 5
Calculated densities of the AlCrFeNi – TiO_2 HEA composites.

Sample Designation	Theoretical density (g/cm^3)	Experimental density (g/cm^3)	Relative density (%)
AlCrFeNi	5.3262	5.3055	99.61136
AlCrFeNi ($2TiO_2$)	5.2988	5.2582	99.23379
AlCrFeNi ($4TiO_2$)	5.2717	5.2096	98.82201
AlCrFeNi ($6TiO_2$)	5.2447	5.1679	98.53566
AlCrFeNi ($8TiO_2$)	5.2181	5.1278	98.26949

demonstrates a notable presence of Al and Ni, following the B2 NiAl phase confirmed by XRD. These findings indicate that the phase composition of the AlCrFeNi prepared using MA and SPS remains consistent with the as-cast AlCrFeNi [23]. Despite a high relative density of 99.6 % in the HEA, the presence of porosities in the composite suggests that challenges during the sample preparation process, such as inadequate compaction, powder contamination, insufficient sintering, or inadequate debinding, could have contributed to the formation of voids [45].

Fig. 11(a-d) illustrates the microstructures of AlCrFeNi reinforced with varying weights of TiO_2 (2, 4, 6, and 8 wt%). Within these microstructures, magnified images of the composite's structure are incorporated. The microstructures consist of two phases: BCC and B2. Furthermore, an interstitial dark phase is observed between the BCC and B2 phases. SEM analyses have verified the homogeneous distribution of the TiO_2-rich phase within the BCC and B2 phases of the AlCrFeNi HEAs. The presence of TiO_2-rich phases is observed to increase proportionally with the increment in TiO_2 particles, ranging from 2 wt% to 8 wt%. Similar studies have reported the formation of metallic oxide (TiO) in HEAs when titanium replaces manganese during the sintering process [46]. Moravcik et al. also documented the presence of dark oxide-rich phases while processing CoCrFeMnNi HEA [47]. In another study, Zhu et al. produced a TiC-dispersed FeCoNiCuAl HEA using high-energy planetary ball milling followed by SPS. SEM analyses confirmed the even distribution of the TiC phase in the FCC and BCC structures of the FeCoNiCuAl HEAs [48].

An area analysis using SEM-EDS was conducted to gain further insights into the microstructure and chemical composition of the phases within the HEA composites. The SEM-EDS analysis of the AlCrFeNi (TiO2) composite is presented in Fig. 12, revealing a precise distribution of elements in the HEA. Fig. 12 demonstrates the composite's uniform Al, Cr, Fe, and Ni distribution. Notably, Cr was found in higher abundance compared to the other elements. Furthermore, the EDS analysis revealed increased Ti content as the wt% of TiO_2 in the composite increased. The presence of distinct TiO_2 particles in the microstructure and the observation of elevated Ti and oxygen (O) content levels strongly suggest that the elements did not decompose during the sintering process. This finding reinforces the integrity of the composite's chemical composition and the presence of well-dispersed TiO_2 particles within the HEA matrix.

3.6. Density and micro-hardness properties of the sintered AlCrFeNi HEA and its composites

The relative densities of the TiO_2-reinforced HEAs were calculated from the theoretical and experimental densities and presented in Table 5. Though the weight of the HEA composites was lighter, their densities were close to the theoretical density of the AlCrFeNi HEA estimated as 5.33 gcm^{-3}. The variation of relative density with TiO_2 addition to HEA is shown in Fig. 13. The relative density is found to be maximum for the unreinforced HEA but decreased with the addition of TiO_2 particles. The reduction in relative density could be linked to poor

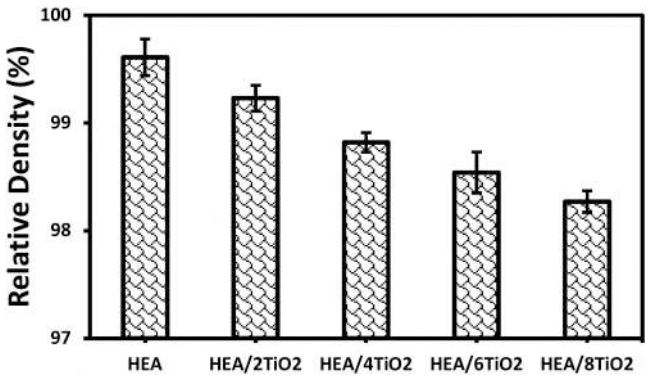

Fig. 13. The variation of relative density of the AlCrFeNi HEA – TiO_2 HEA composites.

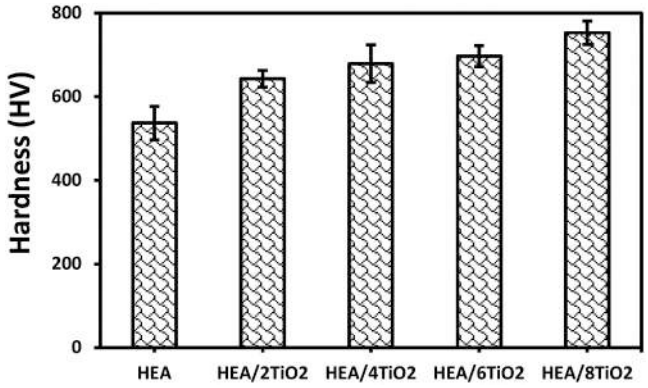

Fig. 14. Graph showing an increase in microhardness of the AlCrFeNi with the addition of TiO_2 from 0 to 8 wt%.

Table 6
Comparison of Vickers hardness of AlCrFeNi and TiO_2 reinforced AlCrFeNi alloys with other studies fabricated by different processing routes.

HEA	Processing Route	Hardness Value (HV)	Source
AlCrFeNi	MA, followed by SPS	537	Present Study
AlCrFeNi(8 wt% TiO_2)	MA, followed by SPS	753	Present Study
AlCrFeNi	Vacuum Arc Melting	472	[51]
AlCrFeNi	Casting	553	[52]
AlCrFeNi	MA, followed by SPS	636	[43]
$Al_{0.75}$CrFeNi	MA, followed by SPS	552	[53]
$Al_{0.6}$CrFeNi	MA, followed by SPS	556	[54]

sinterability and particle agglomeration of the TiO_2 in the HEA composite; this tends to endorse the formation of pores and a consequent decrease in the relative density.

The effect of TiO_2 particle addition on the Vickers hardness of the AlCrFeNi composites is presented in Fig. 14. The addition of TiO_2 particles was noted to improve the resistance to micro indentation during harness testing significantly, which resulted in an increase in hardness value from 537.24 Hv to 752.74 Hv with maximum addition of 8 wt% TiO_2. The hardness of the HEA composite increased with an increase in TiO_2 addition. The improved hardness of the HEA composite could be linked to the high sinter densities of composites (above 98 %), as observed in Fig. 13. The increase in hardness is also attributed to the

harder TiO_2 phase within the AlCrFeNi matrix. TiO_2 particles could act as an impediment to the mobility of dislocation, thereby increasing the resistance to deformation of HEA composites during micro indentation. Similar studies of increased hardness with ceramic reinforcements in HEAs have been reported [49]. For example, Yadav et al. [50] attributed the enhancement in hardness of TiB2-HEA composites to the combined effect of reduced grain size, sinter density, and dispersion hardening effect of TiB_2 particles. Table 6 summarizes the hardness values reported in the literature for AlCrFeNi HEAs. Comparing the results, it is evident that the AlCrFeNi(TiO2) HEA produced in this study through MA and SPS exhibits significantly higher hardness than those produced by casting and vacuum arc melting (VAC). This notable increase in hardness can be attributed to a high concentration of TiO_2, which effectively hinders dislocation movement. Among the samples investigated, the AlCrFeNi alloy reinforced with 8 wt% TiO_2 has the highest hardness (753 HV), demonstrating that its incorporation is a promising approach to enhancing the hardness of AlCrFeNi HEAs. These findings shed light on the development of high-performance HEAs.

4. Conclusions

Our work used Thermo-Calc as a design guide to developing AlCrFeNi HEA and investigated the role of varying percentages of TiO_2 reinforcements on the densification behavior, phase changes, microstructure, and properties of AlCrFeNi HEA fabricated using MA and SPS techniques. Based on the findings, the following conclusions were made:

1. The predicted stable phases for the quaternary equiatomic AlCrFeNi HEA are BCC_B2 and BCC_B2#2 phases. A BCC_B2#3 phase precipitated at 710 °C but later dissolved into the BCC_B2#2 stable phase. The Ω, ΔH, Δχ, and VEC for AlCrFeNi are 0.87, − 21.02, 0.12, and 6.75, respectively, which confirms that the HEA meets the reported criteria for the formation of solid solutions.
2. During densification, a drastic reduction in shrinkage rate from 0.74 to 0.42 was evident with adding 2 wt% TiO_2 particles. The TiO_2 slows the rate of electron discharge that is liable to initiate local heating of particles, lowering the rate of melting of the particle surface.
3. Based on XRD and SEM results, the AlCrFeNi alloy forms a disordered BCC phase rich in Fe, Cr, and an ordered B2 phase rich in Ni, Al. Incorporating TiO_2 resulted in the diffusion of Ti with O atoms fitting into the interstitial sites in the BCC and B2 lattice.
4. The density decreased from 99.61 % to 98.27 % by adding 8 wt% TiO_2. The hardness of reinforced AlCrFeNi is enhanced from 537.24 Hv to 752.74 Hv with an increment of TiO_2 from 0 to 8 wt%. The AlCrFeNi exhibits significantly higher hardness than those produced by casting and vacuum arc melting (VAC).

CRediT authorship contribution statement

Samuel R. Oke: Conceptualization, Investigation, Writing – original draft. **Oluwasegun E. Falodun:** Methodology, Writing – review & editing. **Abiodun Bayode:** Project administration, Resources. **Peter A. Olubambi:** Resources, Supervision.

Declaration of Competing Interest

The authors declare that they have no known competing financial interests or personal relationships that could have appeared to influence the work reported in this paper.

Data availability

Data will be made available on request.

References

[1] L. Zong, L. Xu, C. Luo, Z. Jiao, X. Li, W. Sun, S. Wei, Mechanical properties and strengthening mechanism of the nano-sized m-ZrO2 ceramic particle reinforced NbMoTaW refractory high-entropy alloy, Int. J. Refract. Met. Hard Mater. 113 (2023), 106201.

[2] Z. Yuan, H. Liu, Z. Ma, X. Ma, K. Wang, X. Zhang, Microstructure and properties of high entropy alloy reinforced titanium matrix composites, Mater. Charact. (2022), 111856.

[3] G. Zhang, X. Yang, Y. Zhao, Z. Yang, J. Li, Microstructure and mechanical properties regulation and control of in-situ TiC reinforced CoCrFeNiAl0.2 high-entropy alloy matrix composites via high-gravity combustion route, J. Alloy. Compd. 899 (2022), 163221.

[4] A. Mehta, Y.H. Sohn, Fundamental core effects in transition metal high-entropy alloys: "High-entropy" and "sluggish diffusion" effects, Diffus. Found. 29 (2021) 75–93.

[5] R.K. Nutor, Q. Cao, X. Wang, D. Zhang, Y. Fang, Y. Zhang, J.-Z. Jiang, Phase selection, lattice distortions, and mechanical properties in high-entropy alloys, Adv. Eng. Mater. 22 (2020), 2000466.

[6] B.R. Anne, S. Shaik, M. Tanaka, A. Basu, A crucial review on recent updates of oxidation behavior in high entropy alloys, SN Appl. Sci. 3 (2021) 1–23.

[7] M. Li, Y. Guo, H. Wang, J. Shan, Y. Chang, Microstructures and mechanical properties of oxide dispersion strengthened CoCrFeNi high-entropy alloy produced by mechanical alloying and spark plasma sintering, Intermetallics 123 (2020), 106819.

[8] W. Wu, R. Zhou, B. Wei, S. Ni, Y. Liu, M. Song, Nano-sized precipitates and dislocation networks reinforced C-containing CoCrFeNi high-entropy alloy fabricated by selective laser melting, Mater. Charact. 144 (2018) 605–610.

[9] C. Wu, T. Xu, Z. Wang, C. Zhang, S. Zhang, C. Ni, D. Zhang, Laser surface alloying of FeCoCrAlNiTi high entropy alloy composite coatings reinforced with TiC on 304 stainless steel to enhance wear behavior, Ceram. Int. 48 (2022) 20690–20698.

[10] C. Zhang, J. Zhu, G. Zhang, Y. Hu, Laser powder bed fusion of nano-TiB2 reinforced FeCoNiCr high-entropy alloy with enhanced strength and firm corrosion resistance, J. Alloy. Compd. 927 (2022), 167110.

[11] S.W. Hussain, M.A. Mehmood, M.R.A. Karim, A. Godfrey, K. Yaqoob, Microstructural evolution and mechanical characterization of a WC-reinforced CoCrFeNi HEA matrix composite, Sci. Rep. 12 (2022) 9822.

[12] G. Yan, M. Zheng, Z. Ye, J. Gu, C. Li, C. Wu, B. Wang, In-situ Ti (C, N) reinforced AlCoCrFeNiSi-based high entropy alloy coating with functional gradient double-layer structure fabricated by laser cladding, J. Alloy. Compd. 886 (2021), 161252.

[13] E. Reverte, C. Keller, M. Calvo-Dahlborg, G. Alcalá, M. Campos, J. Cornide, Effect of Y2O3 addition on the microstructure and mechanical properties of an Al1. 8CoCrCu0. 5FeNi BCC HEA, J. Alloy. Compd. 960 (2023), 170647.

[14] H. Qi, G.-l Li, W. Zhang, Q.-y Lü, R.-d Li, S.-c Xie, Y. Shi, B. Yu, R.-r Chen, Y.-d Qu, Effect of TiO2 nano-ceramic particles on microstructure and mechanical properties of Al0. 4CoCrFe2Ni2 high-entropy alloy, China Foundry 19 (2022) 528–534.

[15] Z. Zhang, B. Zhang, S. Zhu, Y. Yu, Z. Wang, X. Zhang, B. Lu, Microstructural characteristics and enhanced wear resistance of nano-scale Al2O3/13 wt% TiO2-reinforced CoCrFeMnNi high entropy coatings, Surf. Coat. Technol. 412 (2021), 127019.

[16] S. Sivasankaran, E.-S.M. Sherif, H.R. Ammar, A.S. Alaboodi, A.-bH. Mekky, Influence of oxide dispersions (Al2O3, TiO2, and Y2O3) in CrFeCuMnNi high-entropy alloy on microstructural changes and corrosion resistance, Crystals 13 (2023) 605.

[17] S. Zhu, Z. Zhang, B. Zhang, Y. Yu, Z.-z Wang, X.C. Zhang, B. Lu, Microstructure and Properties of Al2O3–13 wt%TiO2-Reinforced CoCrFeMnNi high-entropy alloy composite coatings prepared by plasma spraying, J. Therm. Spray. Technol. 30 (2021) 772–786.

[18] W.-C. Chang, Y.-C. Lu, C.-H. Hsueh, Oxide dispersion strengthening of CoCrNi medium entropy alloy using TiO2 particles, Mater. Sci. Eng. A 859 (2022), 144196.

[19] Y.-c Liu, S.-y Yen, S.-h Chu, S.-k Lin, M.-H. Tsai, Mechanical and thermodynamic data-driven design of Al-Co-Cr-Fe-Ni multi-principal element alloys, Mater. Today Commun. 26 (2021), 102096.

[20] M. Ostrowska, P. Riani, B. Bocklund, Z.-K. Liu, G. Cacciamani, Thermodynamic modeling of the Al-Co-Cr-Fe-Ni high entropy alloys supported by key experiments, J. Alloy. Compd. 897 (2022), 162722.

[21] X. Jin, J. Bi, L. Zhang, Y. Zhou, X. Du, Y. Liang, B. Li, A new CrFeNi2Al eutectic high entropy alloy system with excellent mechanical properties, J. Alloy. Compd. 770 (2019) 655–661.

[22] A. Munitz, S. Salhov, G. Guttmann, N. Derimow, M. Nahmany, Heat treatment influence on the microstructure and mechanical properties of AlCrFeNiTi0. 5 high entropy alloys, Mater. Sci. Eng. A 742 (2019) 1–14.

[23] M. Wang, Z. Wen, B. Ma, J. Liu, Z. Zou, Y. Zhao, Enhancing the strength of AlCrFeNi HEAs via tailoring aluminum content and optimal aging treatment, J. Alloy. Compd. 893 (2022), 162242.

[24] E. Jumaev, M.A. Abbas, S.C. Mun, G. Song, S.-J. Hong, K.B. Kim, Nano-scale structural evolution of quaternary AlCrFeNi based high entropy alloys by the addition of specific minor elements and its effect on mechanical characteristics, J. Alloy. Compd. 868 (2021), 159217.

[25] H. Wu, J. Xie, H.-Y. Yang, D.-L. Shu, G.-C. Hou, J.-G. Li, Y.-Z. Zhou, X.-F. Sun, Comparative study of mechanical and corrosion behaviors of cost-effective AlCrFeNi high entropy alloys, J. Mater. Eng. Perform. 31 (2022) 4472–4482.

[26] K.K. Alaneme, M.O. Bodunrin, S.R. Oke, Processing, alloy composition and phase transition effect on the mechanical and corrosion properties of high entropy alloys: a review, J. Mater. Res. Technol. 5 (2016) 384–393.

[27] B.-r Ke, Y.-c Sun, Y. Zhang, W.-r Wang, W.-m Wang, P.-y Ma, W. Ji, Z.-y Fu, Powder metallurgy of high-entropy alloys and related composites: a short review, Int. J. Miner. Metall. Mater. 28 (2021) 931–943.
[28] S.R. Oke, O.O. Ige, O.E. Falodun, A.M. Okoro, M.R. Mphahlele, P.A. Olubambi, Powder metallurgy of stainless steels and composites: a review of mechanical alloying and spark plasma sintering, Int. J. Adv. Manuf. Technol. 102 (2019) 3271–3290.
[29] S.R. Oke, M.R. Mphahlele, O.O. Ige, O.E. Falodun, A.M. Okoro, P.A. Olubambi, Structural characterization and nanoindentation studies on mechanical properties of spark plasma sintered duplex stainless steel nanocomposite, J. Alloy. Compd. 840 (2020), 155648.
[30] S.R. Oke, O.O. Ige, O.E. Falodun, A.M. Okoro, M.R. Mphahlele, P.A. Olubambi, Influence of TiN nanoparticle addition on microstructure and properties of Fe22Cr alloy fabricated by spark plasma sintering, Int. J. Adv. Manuf. Technol. 103 (2019) 4529–4540.
[31] P.S. Ocaño, S.G. Fries, I. Lopez-Galilea, R.D. Kamachali, J. Roik, L.A. Jácome, The AlMo0. 5NbTa0. 5TiZr refractory high entropy superalloy: experimental findings and comparison with calculations using the CALPHAD method, Mater. Des. 217 (2022), 110593.
[32] L. Wang, R.D. Kamachali, CALPHAD integrated grain boundary co-segregation design: towards safe high-entropy alloys, J. Alloy. Compd. 933 (2023), 167717.
[33] N. Shah, M. Rahul, G. Phanikumar, Accelerated design of eutectic high entropy alloys by ICME approach, Metall. Mater. Trans. A 52 (2021) 1574–1580.
[34] J.W. Yeh, S.K. Chen, S.J. Lin, J.Y. Gan, T.S. Chin, T.T. Shun, C.H. Tsau, S.Y. Chang, Nanostructured high-entropy alloys with multiple principal elements: novel alloy design concepts and outcomes, Adv. Eng. Mater. 6 (2004) 299–303.
[35] Y. Zhang, X. Yang, P. Liaw, Alloy design and properties optimization of high-entropy alloys, JOM 64 (2012) 830–838.
[36] Z. Liu, S. Guo, X. Liu, J. Ye, Y. Yang, X.-L. Wang, L. Yang, K. An, C.T. Liu, Micromechanical characterization of casting-induced inhomogeneity in an Al0. 8CoCrCuFeNi high-entropy alloy, Scr. Mater. 64 (2011) 868–871.
[37] Y. Zhao, J. Qiao, S. Ma, M. Gao, H. Yang, M. Chen, Y. Zhang, A hexagonal close-packed high-entropy alloy: the effect of entropy, Mater. Des. 96 (2016) 10–15.
[38] X. Zhang, N. Zhao, C. He, The superior mechanical and physical properties of nanocarbon reinforced bulk composites achieved by architecture design–a review, Prog. Mater. Sci. 113 (2020), 100672.
[39] E. Macía, A. García-Junceda, M. Serrano, S. Hong, M. Campos, Effect of mechanical alloying on the microstructural evolution of a ferritic ODS steel with (Y–Ti–Al–Zr) addition processed by Spark Plasma Sintering (SPS), Nucl. Eng. Technol. 53 (2021) 2582–2590.
[40] H. Ziaei, N. Ebrahimzadeh, Z. Marfavi, B. Sadeghi, P. Cavaliere, Crystal structure evolution in mehcanical alloying and spark plasma sintering of AlxCoCrCuFeNi HEAs, Powder Metall. 64 (2021) 54–63.
[41] S.R. Oke, O.E. Falodun, B.G. Motsa, O.O. Ige, P.A. Olubambi, Spark plasma sintering of Al-Ti-Al2O3 composite, Mater. Today Proc. 18 (2019) 3946–3951.
[42] S.R. Oke, O.E. Falodun, M.R. Mahlatse, O.O. Ige, P.A. Olubambi, Investigation on densification and microstructure of Al-TiO2 composite produced by Spark plasma sintering, Mater. Today Proc. 18 (2019) 3182–3188.
[43] S. Peng, J. Hou, L. Yu, Z. Lu, Effects of sintering temperature and Y2O3/Ti addition on microstructure and hardness of ODS-AlCrFeNi HEAs, Intermetallics 143 (2022), 107469.
[44] S.R. Oke, O.O. Ige, O.E. Falodun, P.A. Olubambi, J. Westraadt, Densification and grain boundary nitrides in spark plasma sintered SAF 2205-TiN composite, Int. J. Refract. Met. Hard Mater. 81 (2019) 78–84.
[45] A. Mussatto, R. Groarke, R.K. Vijayaraghavan, C. Hughes, M.A. Obeidi, M.N. Doğu, M.A. Yalçin, P.J. McNally, Y. Delaure, D. Brabazon, Assessing dependency of part properties on the printing location in laser-powder bed fusion metal additive manufacturing, Mater. Today Commun. 30 (2022), 103209.
[46] P. Satyanarayana, R. Sokkalingam, P. Jena, K. Sivaprasad, K. Prashanth, Tungsten matrix composite reinforced with cocrfemnni high-entropy alloy: impact of processing routes on microstructure and mechanical properties, Metals 9 (2019) 992.
[47] I. Moravcik, J. Cizek, Ld.A. Gouvea, J. Cupera, I. Guban, I. Dlouhy, Nitrogen interstitial alloying of CoCrFeMnNi high entropy alloy through reactive powder milling, Entropy 21 (2019) 363.
[48] T. Zhu, H. Wu, R. Zhou, N. Zhang, Y. Yin, L. Liang, Y. Liu, J. Li, Q. Shan, Q. Li, Microstructures and tribological properties of TiC reinforced FeCoNiCuAl high-entropy alloy at normal and elevated temperature, Metals 10 (2020) 387.
[49] W. Ji, J. Zhang, W. Wang, H. Wang, F. Zhang, Y. Wang, Z. Fu, Fabrication and properties of TiB2-based cermets by spark plasma sintering with CoCrFeNiTiAl high-entropy alloy as sintering aid, J. Eur. Ceram. Soc. 35 (2015) 879–886.
[50] S. Yadav, A. Aggrawal, A. Kumar, K. Biswas, Effect of TiB2 addition on wear behavior of (AlCrFeMnV) 90Bi10 high entropy alloy composite, Tribol. Int. 132 (2019) 62–74.
[51] Y. Dong, Y. Lu, J. Kong, J. Zhang, T. Li, Microstructure and mechanical properties of multi-component AlCrFeNiMox high-entropy alloys, J. Alloy. Compd. 573 (2013) 96–101.
[52] Z. Jiang, W. Chen, Z. Xia, W. Xiong, Z. Fu, Influence of synthesis method on microstructure and mechanical behavior of Co-free AlCrFeNi medium-entropy alloy, Intermetallics 108 (2019) 45–54.
[53] Z. Fu, W. Chen, H. Wen, Z. Chen, E.J. Lavernia, Effects of Co and sintering method on microstructure and mechanical behavior of a high-entropy Al0. 6NiFeCrCo alloy prepared by powder metallurgy, J. Alloy. Compd. 646 (2015) 175–182.
[54] Z. Chen, W. Chen, B. Wu, X. Cao, L. Liu, Z. Fu, Effects of Co and Ti on microstructure and mechanical behavior of Al0. 75FeNiCrCo high entropy alloy prepared by mechanical alloying and spark plasma sintering, Mater. Sci. Eng. A 648 (2015) 217–224.